CryoEM map of *Pseudomonas aeruginosa* PilQ enables structural characterization of TsaP

Matthew McCallum[1,2,†,‡], Stephanie Tammam[1,†], John L. Rubinstein[1,2,3,*], Lori L. Burrows[4,*], P. Lynne Howell[1,2,*]

[1]Program in Molecular Structure & Function, Peter Gilgan Centre for Research and Learning, The Hospital for Sick Children, Toronto, ON M5G 0A4, Canada.

[2]Department of Biochemistry, University of Toronto, Toronto, ON M5S 1A8, Canada

[3]Department of Medical Biophysics, University of Toronto, Toronto, ON M5G 1l7, Canada.

[4]Department of Biochemistry and Biomedical Sciences and the Michael G. DeGroote Institute for Infectious Disease Research, McMaster University, Hamilton, ON L8S 4K1, Canada.

[*]To whom correspondence should be addressed:

howell@sickkids.ca, lori.burrows@mcmaster.ca, john.rubinstein@utoronto.ca

Lead contact: PLH

[†]These authors contributed equally to this work

[‡]Current address: Department of Biochemistry, University of Washington, Seattle, WA 98195-7350, USA.

ABSTRACT

The type IV pilus machinery is a multi-protein complex that polymerizes and depolymerizes a pilus fibre used for attachment, twitching motility, phage adsorption, natural competence, protein secretion, and surface-sensing. An outer membrane secretin pore is required for passage of the pilus fibre out of the cell. Herein, the structure of the tetradecameric secretin, PilQ, from the *Pseudomonas aeruginosa* type IVa pilus system was determined to 4.3 Å and 4.4 Å resolution in the presence and absence of C_7 symmetric spokes, respectively. The heptameric spokes were found to be the two tandem C-terminal domains of TsaP. TsaP forms a belt around PilQ and while the protein is not essential for twitching motility, over-expression of TsaP triggers a signal cascade upstream of PilY1 leading to cyclic di-GMP up-regulation. These results resolve the identity of the spokes identified with Proteobacterial PilQ homologs and may reveal a new component of the surface-sensing cyclic di-GMP signal cascade.

IMPACT STATEMENT

The type IV pilus is critical for bacterial virulence. The co-structure of the pilus secretin PilQ and TsaP is determined. Characterization of TsaP implicates it in surface-sensing signal transduction.

INTRODUCTION

The type IVa pilus (T4aP) facilitates many bacterial functions including attachment, twitching motility, phage adsorption, natural competence, protein secretion, and surface-sensing[1,2]. The surface-sensing role of T4aP is of particular interest due to its involvement in the up-regulation of cyclic di-GMP – the master regulator of biofilm formation[3,4]. Biofilms are of critical medical and industrial importance, as they increase bacterial tolerance of otherwise uninhabitable conditions, antibiotics, and to the immune system[5].

The T4aP machinery comprises a cell envelope-spanning multi-protein complex. This machinery polymerizes long thin fibres that attach to surfaces and retract to pull bacteria towards the point of attachment[1,2]. The pilus is a polymer mainly composed of the major subunit, PilA. At the pilus base, the inner membrane protein PilC and cytoplasmic ATPase motors, PilB and PilT, catalyze polymerization and depolymerization, respectively[6,7]. Minor pilins and PilY1 initiate pilus polymerization and are thus thought to localize at the pilus tip[8,9]. The pilus exits the periplasm through an outer membrane pore formed by PilQ oligomers. The PilQ pore is aligned

with the motors by a subcomplex of PilM, PilN, PilO, and PilP[10,11]. PilF shuttles PilQ to the outer membrane and facilitates its oligomerization. PilMNOP, PilY1, and PilT are all required for T4aP-mediated surface sensing [12,13]. It is unclear whether other proteins that are part of the T4aP apparatus and interface with PilM, PilN, PilO, and PilP – such as PilQ – are also needed for surface sensing.

PilQ and PilF are the secretin and pilotin of the T4aP, respectively. Secretins and their cognate pilotins create outer-membrane channels in various secretion and pilus systems. Secretin oligomers have a unique double-layered β-barrel architecture[14,15]. The outer β-barrel forms a large vestibule that passes though the outer membrane[15]. The inner β-barrel curves inwards to form a gate at the midway point of the secretin β-barrel[15]. Domains N1 and N0 form rings below the β-barrel[15]. PilQ secretins from Proteobacteria, structurally characterized at low resolution, show radial spokes emerging from a central barrel[16-19]. Models of PilQ from *Thermus thermophilus* ($PilQ^{Tt}$) and *Vibrio cholerae* ($PilQ^{Vc}$) competence pilus systems – which are divergent from Proteobacterial T4aP secretins – were recently built into 7 and 2.7 Å resolution electron cryomicroscopy (cryoEM) maps, respectively [20,21]. These competence secretins lack the lip subdomain and the radial spokes found in T4aP secretins.

Structures of the related type II secretion system (T2SS) secretins also have radial spokes[22,23]. These structures were determined at 3-4 Å resolution, permitting modeling of the spoke protein as the T2SS pilotin[22,23]. This finding suggests that the spokes in the T4aP structures could be the T4aP pilotin, PilF. However, PilF is structurally unrelated to the T2SS pilotin, and other studies indicate that the spokes are most likely the protein TsaP[16,19]. 2D class averages of cryoEM particles embedded in purified *Neisseria* sp. membranes show spokes around the PilQ barrel, and these spokes disappear upon deletion of TsaP[16]. Similarly, electron cryotomography of *Myxococcus xanthus* show that density consistent with the location of the spokes around PilQ disappears upon deletion of TsaP[19]. Little is known about the molecular function of TsaP, except that it has a LysM domain characteristic of septal peptidoglycan binding[16]. Neither TsaP nor PilF are not expressed in the same operon as PilQ.

We previously resolved a 7.4 Å map of PilQ from *Pseudomonas aeruginosa* ($PilQ^{Pa}$) with presumed tetradecameric stoichiometry and C_7 symmetric spoke density[18]. Although this was the highest resolution structure of a secretin at that time, it was not sufficient for model building. Herein, our reprocessing of those micrographs with improved image analysis and model-building

83 algorithms yielded three distinct structures of PilQ^{Pa}. These maps were of sufficient resolution to
84 enable building of an atomic model. Mass spectrometry revealed the identity of the protein bound
85 in the spoke density to be TsaP, and a TsaP model was readily built into the spoke density. While
86 probing for the function of TsaP, we found that that its overexpression triggers cyclic di-GMP
87 up-regulation upstream of PilY1, implicating a role in the T4aP-dependent surface-sensing signal
88 cascade.
89
90 **RESULTS**
91 **PilQ^{Pa} forms tetradecameric and pentadecameric barrels**
92 We previously resolved a 7.4 Å resolution PilQ^{Pa} cryoEM map[18]. Using the template-
93 based automatic particle selection algorithm implemented in cryoSPARC v.2[24], eight times more
94 particles were selected automatically from the original micrographs than when particle selection
95 was performed manually (**Supplementary Table 1**). *Ab initio* classification followed by
96 heterogeneous particle refinement in 3D revealed three unique classes, with 44 % of particle
97 images classified as C_{14} symmetric barrels with C_7 symmetric radial spokes (**Figure 1A)**, 48 % of
98 particle images classifying as C_{14} symmetric barrels without spokes (**Figure 1B)**, and 8 % as C_{15}
99 symmetric barrels without spokes (**Figure 1C**). Refining the three classes yielded maps at 4.3,
100 4.4, and 6.9 Å resolution, respectively. The distinct C_{14} and C_{15} symmetric maps identified are
101 reminiscent of the finding that the T2SS secretin can have more than one symmetry[25].
102 Local resolution in the barrel of the 4.3 and 4.4 Å maps is estimated to be 3.5 Å. The
103 secondary structure and large side chains were visible in the map and enabled model building of
104 14 PilQ^{Pa} N1 and secretin domains (**Figure 1A**). Although we verified that the N0 and
105 peptidoglycan-binding AMI_N domains of PilQ were present using mass spectrometry analyses
106 (**Supplementary Figure 1**), they could not be modeled, consistent with these domains adopting
107 random orientations relative to the secretin barrel in the absence of the peptidoglycan and the rest
108 of the T4aP apparatus. Protomers of the barrel structure from the spoked barrel map were fit into
109 the maps of the C_{14} and C_{15} barrels without spokes and refined.
110 The final models were compared to co-evolved residues within PilQ^{Pa} homologs as
111 identified by the EVcouplings webserver[26]. Residues in proximity to one another in a structure
112 develop complementary mutations as the protein evolves[27]. These co-evolved residues can be
113 used to independently predict and validate the conformations of proteins[27]. We found a clear

114 correlation between the co-evolved residues and the N1 and secretin domains, validating these
115 structures (**Figure 1D**). The sequence of the lip subdomain is not well conserved in PilQ, and the
116 poor sequence alignment in this region yielded fewer co-evolved residues in the lip subdomain
117 (**Figure 1D**).
118
119 **Co-evolved residues are consistent with secretin gate and barrel dynamics**
120 Co-evolved residues not directly supported by the model of $PilQ^{Pa}$ were also identified,
121 suggesting dynamics not visualized in the cryoEM maps. There are co-evolved residues between
122 the secretin gate and the secretin barrel (**Figure 1E**), consistent with a swinging gate-like model
123 of secretin gate opening demonstrated recently for the secretin from the type III secretion
124 injectisome, InvG[28]. Residue G577 is located at the proposed hinge of the *P. aeruginosa* PilQ
125 secretin gate (**Figure 1E**). Mutation of the corresponding residue in *M. xanthus* PilQ (G764S)
126 causes vancomycin sensitivity[29] presumably because the hinge of the gate is jammed open
127 permitting entry of the bulky antibiotic across the outer membrane. This hypothesis is supported
128 by the structure of a mutant of the T2SS secretin where the corresponding residue G458 was
129 changed to alanine (G458A)[25]. The G458A T2SS secretin structure reveals a partially open
130 secretin gate[25].
131 Co-evolved residues were also identified at the top of the secretin barrel and near the
132 bottom of the secretin barrel, adjacent to the secretin gate (**Figure 1F**). These co-evolved residues
133 may be consistent with the secretin barrel folding such that the top of the secretin barrel covers
134 the gate-adjacent segment of the secretin. The top of the secretin is hydrophobic (**Figure 1G**),
135 like other secretin structures[15], consistent with this region being the site for outer membrane
136 insertion. Thus, one explanation for these co-evolved residues may be that a folding intermediate
137 positions the top of the secretin barrel to mask these hydrophobic sites prior to membrane
138 insertion (**Figure 1F**). The gate-adjacent section of the secretin barrel is highly conserved
139 (**Figure 1G**) and provides the interface for the spoke density. Once PilQ inserts into the outer
140 membrane and this region becomes exposed, the spoke protein could bind and stabilize the PilQ
141 oligomer.
142
143 **Dynamics in the secretin gates visualized**

144 The conformations of the secretin gates in the C_{15}, C_{14}, and spoked C_{14} PilQ^{Pa} barrels are
145 different. While the secretin gate in the C_{15} barrels is perpendicular to the walls of the barrel, the
146 secretin gate in the C_{14} barrel invaginates towards the periplasm. Comparing the C_{15} and C_{14}
147 barrels without spokes, the residues at the center of the secretin gate are displaced by 4 Å (**Figure**
148 **1B-C, Animation 1**). This invagination is likely the result of the 5 Å reduction in diameter of the
149 tetradecameric barrel relative to the pentadecameric form, leaving less room for the gate to
150 extend perpendicularly from the walls of the barrel.
151 Comparing the C_{14} and spoked C_{14} barrels reveals that the secretin gate invaginates by an
152 additional 3 Å in the spoked C_{14} barrel (**Figure 1A-B**). A smaller barrel diameter cannot explain
153 this movement, as the diameters of the C_{14} barrel and spoked C_{14} barrels are identical. Comparing
154 the C_{15}, C_{14}, and spoked C_{14} barrels reveals a pivot point for gate invagination in the secretin
155 barrel adjacent to the secretin gate and the spokes (**Figure 1H-I and Animation 1**). This finding
156 is consistent with the molecules bound at the spokes promoting secretin gate invagination.
157
158 **TsaP co-purifies with PilQ**
159 There are two features in the maps of PilQ^{Pa} that cannot be explained by models of PilQ^{Pa}
160 alone. First are the C_7 symmetric spokes. The spoke density appears to be comprised of 14
161 structurally similar β-roll protein structures that form a belt around PilQ. There are differences in
162 every other β-roll that give the spokes C_7 symmetry (**Figure 1A**). There is also extra density
163 beneath the secretin gate that plugs the small opening in the center of both tetradecameric PilQ
164 barrels – the density is more pronounced in the spoked tetradecameric barrel map (**Figure 1A-B**).
165 The local quality of the map beneath the secretin gate is too poor to identify distinct structural
166 elements. Curiously, there is no evidence of C_{15} barrels with spokes or extra density beneath the
167 secretin gates, hinting at stoichiometry-dependent interactions.
168 To identify the protein(s) that constitute the extra densities, mass spectrometry was
169 performed on the protein sample used for cryoEM grid preparation. Aside from PilQ^{Pa}, the most
170 abundant components are PrpL, PA5122, and TsaP (**Supplementary Table 2, Supplementary**
171 **Figure 2**). TsaP is the protein most likely responsible for the spoke density as it has been shown
172 to be critical for PilQ spoke visualization in *Neisseria* sp. and *M. xanthus*[16,19]. PrpL is an
173 extracellular protease secreted by the T2SS[30,31] and thus unlikely to constitute these densities.
174 PA5122 is an uncharacterized protein with a secretion signal sequence.

175

176 **Model building of TsaP reveals unique heptamer structure**

177 The structure of TsaP is not known; however, TsaP was predicted to have an N-terminal
178 peptidoglycan-binding LysM domain linked by unstructured residues to a C-terminal domain[19].
179 The C-terminal domain of TsaP, henceforth referred to as the CII domain, was predicted to be
180 similar to the C-domain of the flagellar ring-forming component, FlgT[19]. The C-domain of FlgT
181 has a β-roll structure with an extruding finger subdomain[32] and the Phyre[2] structure prediction of
182 TsaP from *P. aeruginosa* is consistent with this fold (**Figure 2A**). To validate this result, TsaP
183 co-evolved residues identified by the EVcouplings webserver[26] were compared with the predicted
184 structure of the TsaP CII domain (**Figure 2B**). The correlations between co-evolved residues and
185 residues close to one another in the CII domain structure prediction provide support for its
186 similarity to the FlgT C-domain. Inspection of TsaP co-evolved residues revealed a duplicate
187 pattern of co-evolved residues preceding the CII domain (**Figure 2B**), consistent with a second
188 domain with a similar structure, henceforth referred to as the CI domain. When the structure of
189 the CI domain segment was predicted[33,34] we found that it was also similar to the FlgT C-domain
190 (**Figure 2A**). This is distinct from previous predictions that identified only a single C-domain in
191 TsaP[19].

192 The β-roll structure and extruding finger subdomain in the CI and CII models can be
193 clearly seen in the spoke density (**Figure 2C**). There is also density consistent with linker
194 residues preceding the CI domain and between the CI and CII domains. In contrast, Phyre[2]
195 predicted structures of PrpL and PA5122 do not fit the size or shape of the spokes. The C-
196 terminal 224 residues of TsaP encompassing the CI and CII domains were therefore modeled and
197 refined into the map. This model reveals that TsaP forms a heptameric ring with C_7 symmetry
198 around $PilQ^{Pa}$ at the midpoint of the barrel where the internal gate is positioned (**Figure 2D**).
199 Each finger subdomain contacts the adjacent C domain to mediate intramolecular CI^n-CII^n
200 interactions and intermolecular CII^n-CI^{n+1} interactions. These finger subdomain interactions
201 correlate with co-evolved residue pairs in TsaP (**Figure 2B**), further validating the model of TsaP
202 built into this map.

203 Each C domain contacts a separate PilQ protomer. The buried surface area of the TsaP-
204 PilQ interaction is 2924 $Å^2$ per TsaP protomer, or 20468 $Å^2$ for the entire 7:14 TsaP-PilQ
205 interaction. The buried surface area of the TsaP-TsaP oligomeric interface is 913 $Å^2$. The larger

206 buried surface area of the TsaP-PilQ interface compared with the TsaP-TsaP oligomeric interface
207 hints that the PilQ interaction may help facilitate TsaP oligomerization.
208
209 **Overexpression of TsaP triggers cyclic di-GMP signalling**
210 *tsaP* mutants have a 40 % defect in twitching motility, which can be complemented *in*
211 *trans* by leaky expression from *tsaP* under an arabinose-inducible promotor without the addition
212 of arabinose (**Figure 3A**). We previously reported finding no obvious defect in twitching motility
213 with the *tsaP* mutant[18]; this was likely the result of a limited number of replicates combined with
214 the modest phenotype. Compared to the vector control, a 66 % defect in twitching motility is
215 observed in wild-type *P. aeruginosa* or the *tsaP* mutant complemented with *tsaP* when induced
216 with 0.1 % (w/v) arabinose – henceforth referred to as over-expressed TsaP (**Figure 3B**) –
217 consistent with both deletion and over-expression of TsaP impairing twitching motility.
218 We also assessed the propensity of *tsaP* mutants and TsaP-overexpressing *P. aeruginosa*
219 to form biofilms, using a Congo red dye uptake assay. Congo red binds to the Pel polysaccharide
220 in *P. aeruginosa* biofilms, leading to red colonies and a small clear halo around the colonies
221 where the dye has been taken up[35,36]. We found that the *tsaP* deletion mutant is indistinguishable
222 from wild-type *P. aeruginosa* (**Figure 3B**). However, TsaP overexpression in wild type or the
223 *tsaP* mutant leads to red colonies surrounded by pronounced clearing (**Figure 3B**), consistent
224 with the over-expression of TsaP leading to increased biofilm formation.
225 To look at other surface-associated phenotypes, we assessed the propensity of TsaP
226 overexpressing *P. aeruginosa* to secrete proteases using a casein proteolysis assay. Hydrolysis of
227 casein by extracelluar proteases leads to clear halos around protease- secreting colonies on solid
228 skim milk media[37]. Clear halos form around wild-type *P. aeruginosa* and the *tsaP* deletion
229 mutant; however, no halos form around TsaP over-expressing colonies (**Figure 3B**), consistent
230 with its over-expression decreasing extracellular protease secretion.
231 Reduced extracellular protease secretion, decreased twitching motility zones, and
232 increased biofilm formation are all associated with cyclic di-GMP induction[4,38-40]. Measurement
233 of luciferase expression from a cyclic di-GMP sensitive promotor verified that TsaP
234 overexpression increases cellular cyclic di-GMP concentrations (**Figure 3C**). Growth curves
235 confirmed that increased luciferase expression is not a result of increased cell growth (**Figure**

236 **3C**). These results are consistent with TsaP over-expression up-regulating the production of
237 cyclic di-GMP.
238
239 **TsaP signalling occurs upstream of PilY1**
240 We probed the dependency of cyclic di-GMP signal upregulation caused by TsaP-
241 overexpression on other T4aP proteins. Surprisingly, deletion of PilQ or the PilQ pilotin, PilF,
242 did not prevent TsaP over-expression from increasing Congo-red dye uptake (**Figure 3D**). This
243 indicates that PilQ is not downstream of TsaP in this signal cascade. Like TsaP, PilY1 over-
244 expression in *trans* can trigger increased cyclic di-GMP production[12]. Deleting the *pilMNOP*
245 genes blocks cyclic di-GMP induction upon PilY1 over-expression[12]. When TsaP was over-
246 expressed in a *pilY1* deletion mutant, there was decreased Congo-red dye uptake, consistent with
247 TsaP over-expression inducing a signal cascade that proceeds through PilY1 (**Figure 3D**).
248 Likewise, TsaP over-expression in *pilN*, *pilO*, or *pilP* mutants resulted in less Congo red dye
249 uptake (**Figure 3D**). These results are consistent with TsaP over-expression triggering a T4aP-
250 related cyclic di-GMP signal transduction pathway.
251
252 **DISCUSSION**
253 We determined the structure of PilQ alone and bound to TsaP, and found that TsaP over-
254 expression leads to increased expression of cyclic di-GMP, upstream of PilY1. Our results
255 resolve the identity of the spokes identified in Proteobacterial PilQ cryoEM densities and may
256 reveal a new component of the surface-sensing signal cascade.
257 Where most secretins are bound by their cognate pilotin around the periphery of the
258 secretin barrel adjacent to the secretin gate, we found $PilQ^{Pa}$ is bound by TsaP. Unlike pilotins,
259 TsaP is not essential for PilQ assembly or twitching motility[16,18,19]. Where and how the pilotin
260 PilF interacts with PilQ remains an open question, although one possibility is that TsaP replaces
261 PilF after insertion of PilQ into the outer membrane. We identified co-evolved residues that are
262 consistent with the TsaP-binding region of PilQ interacting with the hydrophobic membrane-
263 interacting interface. This hints at a model of PilQ membrane insertion in which secretin
264 monomers initially fold onto themselves, with the TsaP-binding site occluding the hydrophobic
265 membrane insertion site. Binding by pilotins to the TsaP-binding site might then promote the
266 insertion of PilQ into the membrane, rationalizing the necessity of pilotins for secretin assembly

267 and localization. If this were the case, after outer-membrane insertion of PilQ, PilF could be
268 replaced by TsaP.
269 It seems likely that TsaP and PilQ are tightly associated, as the buried surface area of the
270 TsaP-PilQ interaction is enormous (20468 $Å^2$) and the complex is stable in detergent. It is
271 nonetheless possible that some of the TsaP rings were removed during the purification, as only
272 about half of the purified PilQ particles have TsaP associated with them. In this case, PilQ
273 partially bound by TsaP might be expected, but only PilQ entirely bound by TsaP or without
274 TsaP were identified in cryoEM 3D classes. Alternatively, there may be a population of free PilQ
275 oligomers representing an intermediate state between PilQ-PilF and PilQ-TsaP complexes.
276 The structure of PilQ was determined in two distinct stoichiometries. Interestingly, only
277 the tetradecameric form is bound by TsaP and had the unidentified secretin gate plug. The 2:1
278 PilQ:TsaP configuration necessitates binding of only even-numbered PilQ stoichiometries. It may
279 be that TsaP recognizes or selects for specific secretin stoichiometries. Selecting particular
280 secretin stoichiometries may improve the efficiency of T4aP function, consistent with the
281 moderate twitching motility defect of the TsaP-deletion mutant.
282 In addition to influencing the quaternary structure of PilQ, TsaP binding may alter its
283 tertiary structure. Comparing the different PilQ structures revealed a pivot point for secretin gate
284 invagination adjacent to the spokes, consistent with TsaP binding influencing this process. Thus,
285 a plausible role for TsaP may be in modifying secretin-gate invagination. The consequences of
286 this are not clear, but the gate could then interact with the pilus initiation complex of minor pilins
287 and PilY1 and/or the unidentified secretin gate plug.
288 TsaP could also be involved with larger-scale secretin movements. For example, PilQ
289 adopts distinct open and closed states depending on whether the pilus fibre occupies the central
290 channel the T4aP[19,20]. Compared to T4aP maps obtained by electron cryotomography in which
291 the pilus fibre does not occupy the T4aP, the OM in the piliated state has moved 20 Å away from
292 PilP and the peptidoglycan[19]. Although the secretin domain is embedded in the OM, the AMI_N
293 and N0 domains of PilQ bind peptidoglycan and PilP, respectively[41]. This suggests that PilQ
294 must extend and contract 20 Å between the piliated and non-piliated states. As TsaP binds to both
295 the peptidoglycan and secretin domain of PilQ, TsaP binding could modulate secretin opening.
296 For example, TsaP could act as an elastic band between the peptidoglycan and outer-membrane
297 components of PilQ, keeping PilQ contracted and the T4aP closed in the absence of an assembled

298 pilus. The predicted disordered residues between the LysM and CI/CII domains could afford
299 TsaP the elasticity required for this action.
300 Alternatively, instead of modulating PilQ structure, TsaP may sense PilQ conformations
301 and relay this information as a part of a signal cascade. However, while TsaP over-expression
302 triggers the cyclic di-GMP signal cascade, it does so independently of PilQ. This is curious as
303 PilQ provides the only known physical contact between TsaP and PilN, PilO, and PilP – which
304 are important for inducing cyclic di-GMP production. It may be that there is a PilQ-independent
305 signal transduction pathway from TsaP to PilY1 and PilNOP. Alternatively, over-expressing
306 TsaP may force a signalling event that is typically dependent on PilQ. As TsaP has a
307 peptidoglycan-binding LysM domain, overexpression might place strain on the peptidoglycan
308 that resembles what happens during surface interactions, leading to cyclic di-GMP induction. In
309 the absence of a known trigger for the signalling cascade upstream of TsaP, it is not clear what
310 role TsaP plays in the surface-sensing signal cascade under native expression conditions.
311 Nonetheless, knowing that TsaP over-expression can trigger the cyclic di-GMP signal cascade
312 upstream of PilY1 will be useful in identifying other key players in the surface sensing signal
313 cascade.
314
315 **METHODS**
316 **Cloning and mutagenesis**
317 TsaP from *P. aeruginosa* PAO1 was PCR amplified from genomic DNA using primers
318 TsaP_fwd and TsaP_rev (**Supplementary Table 3**), digested with KpnI and XbaI, and cloned into
319 pBADGr to create pBADGr:*tsaP* for arabinose inducible expression of TsaP. Plasmid sequences
320 were verified by TCAG sequencing facilities (The Hospital for Sick Children, Canada).
321
322 **TsaP Deletion**
323 A gene deletion allele was ordered from BioBasic and subcloned into pEX18Gm at the
324 BamHI site producing pEX18Gm_*tsaP*. Clones were confirmed by digest and DNA sequencing
325 (TCAG, The Hospital for Sick Children). The pEX18Gm_*tsaP* construct was transformed into
326 chemically competent SM10 *E. coli* cells, colonies containing pEX18Gm_*tsaP* were mated with
327 mPAO1 using a method described elsewhere[42]. Briefly, after mating *P. aeruginosa* was selected
328 for by growth on LB agar plates containing 25 μg/ml triclosan (Sigma) followed by selection of

329 the merodiploid strains on VBMM agar containing 30 μg/ml gentamicin. Counter selection to
330 resolve the merodiploids was performed on 1.5 % agar plates with 10 g/L tryptone, 5 g/L yeast
331 extract, and 15% (wt/vol) sucrose. The deletion was verified by the absence of a PCR product using
332 primers TsaP_fwd and TsaP_rev.
333
334 **Phenotypic characterizations**
335 *P. aeruginosa* PAO1 with and without deletion mutations of *tsaP*, *pilN*, *pilO*, *pilP*, *pilQ*,
336 *pilY1* were electroporated with pBADGr or pBADGr:tsaP. *P. aeruginosa* PAO1 with and without
337 deletion mutations of *tsaP* were also electroporated with pBADGr:tsaP.
338 Twitching assays were performed as described previously[43,44] except that assays were
339 performed in 150 mm by 15 mm petri polystyrene dishes (Fisher Scientific) with 30 μg/ml
340 gentamicin for 18 h at 37 °C. After this incubation, the agar was then carefully discarded and the
341 adherent bacteria were stained with 1 % (w/v) crystal violet dye, followed by washing with
342 deionized water to remove unbound dye. Twitching zone areas were measured using ImageJ
343 software[45]. Twitching motility assays were performed in six replicates.
344 For Congo-red dye binding assays, cells were grown in 0.5 mL of lysogeny broth (LB) with
345 30 μg/ml gentamicin for 16 h at 37 °C while shaking. Cultures were normalized to an OD at 600
346 nm of 0.1 and then 3 μl of culture was spotted onto Congo red plates (1% (wt/vol) Tryptone, 1%
347 (wt/vol) agar, 0.004% (wt/vol) congo red, and 0.0015% (wt/vol) Coomassie Brilliant Blue R250,
348 and either 0, 0.01, or 0.1% L-arabinose) with the appropriate antibiotic, and grown for 24-36 h at
349 37 °C.
350 Extracellular proteases were assayed using skim milk plates (1% wt/vol agar, 1% wt/vol
351 skim milk powder, and either 0, 0.01, or 0.1% L-arabinose) with the appropriate antibiotic, using
352 the same normalized cultures used for the Congo red binding assays. 3 μl of culture was spotted
353 on a plate and incubated for 16 hrs at 37 °C. All plates were scanned using an Epson Perfection
354 4990 scanner and Epson Scan software.
355 For luciferase expression, cells previously electroporated with pBADGr, pBADGr::tsaP
356 and pBADGr::tsaP mutant constructs were electroporated with pMS402:PcdrA. Cells were grown
357 in 0.5 mL of lysogeny broth (LB) with 30 μg/ml gentamicin and 150 μg/ml kanamycin for 16 h at
358 37 °C while shaking. Cultures were normalized to OD600 of 0.1 and diluted 10x into fresh LB
359 broth containing 30 μg/ml gentamicin, 105 μg/ml kanamycin and either 0, 0.01% or 0.1% L-

360 arabinose in a 384 well plate (Corning, 3821). All samples were done in triplicate. Growth and
361 luciferase activity were monitored over a 16-hour period in a Synergy Neo2 plate reader (BioTek
362 Instruments). Data was analyzed and plotted using Prism 8 (Graph Pad).
363
364 **Plotting the residues at the packing unit interface**
365 CMview[46] was used to identify residues that are near one another. The contact type was set
366 to 'ALL' (i.e. every atom available in the structure) and the distance cut-off was set to 8 Å. To
367 identify residues that are near one another in PilQ monomers, the CI domain of TsaP (residues 126-
368 211), or the CII domain of TsaP (residues 235-324), these structure segments were loaded
369 separately. To identify intra-molecular CI to CII residues that are near each other in TsaP, full-
370 length TsaP was loaded. To identify inter-molecular residues that are near one another, two
371 adjacent PilQ protomers were loaded together, or the CI domain and CII domains from two adjacent
372 protomers were loaded together.
373
374 **Identifying evolutionarily-coupled residues**
375 The TsaP and $PilQ^{Pa}$ amino acid sequences were analyzed using the EVcouplings
376 webserver[26] with default parameters. Homologs were identified, aligned, and analyzed – in total,
377 2642 and 11302 for TsaP and PilQ, respectively. There was poor alignment quality in the lip
378 subdomain of PilQ (residues 481-531) so few evolutionarily-coupled residue pairs were discovered
379 in the lip subdomain. Only residue pairs with a probability score greater than 0.845 or 0.985 were
380 included in subsequent analysis, for TsaP and PilQ, respectively. To better understand the
381 significance of these evolutionarily coupled residues, they were compared to the residues that are
382 near one another identified in CMview.
383
384 **CryoEM analysis**
385 As previously described for this dataset[18], cryoEM data was collected as movies (30 frames
386 over 15 sec) with a FEI Tecnai F20 electron microscope operating at 200 kV and equipped with a
387 Gatan K2 Summit direct detector camera. The exposure rate was 5 electrons/pixel/s with a
388 calibrated pixel size of 1.45 Å/pixel. Previously, movie frames had been aligned with
389 alignframes_lmbfgs[47] and then individual movie frames were discarded for data storage purposes;
390 this prevented exposure weighting and individual particle motion correction herein. Further image

processing here was performed in cryoSPARC v2.8.0[24] (**Supplementary Table 1**). CTF parameters were estimated from the average of aligned frames with CTFFIND4[48] within cryoSPARC and individual particle motion correction and exposure weighting was done with an implementation of alignparts_lmbfgs[47] within cryoSPARC. Initial 2D class averages were generated with manually selected particle images; these class averages were then used to select more particle images. Particle images were extracted in 256×256 pixel boxes then subjected to 2D classification. For the purposes of 3D classification, particle images contributing to 2D classes without high-resolution features were removed. *Ab initio* reconstruction was performed using two classes, revealing barrels and spoked-barrels. The particles contributing to the barrels without spokes were used for an additional round of *ab initio* reconstruction with two classes, revealing an additional class with wider barrels. The spoked barrels, the barrels without spokes, and the wider barrels without spokes were then used as initial models for heterogeneous refinement; particles from 3D classes that did not converge at this stage were removed. Particles from distinct 3D classes were then subjected to non-uniform refinement[49]. The resulting fourier shell correlations for the 4.3 and 4.4 Å maps are unusual as there is a flat region between ~7 Å and ~5 Å. This likely arises from the diffuse density from the detergent layer and the N-terminal domains disordered relative to the secretin of PilQ. However, the clear features from the beta-barrels support the resolution estimates for the maps

A molecular model could be built using Coot[50] into the spoked barrel map using the structures of FlgT and GspD[25,32] as guides for TsaP and PilQ, respectively. Molecular models for the maps of barrels without spokes were built by fitting the PilQ protomers built into the spoked barrel map in Coot[50]. These models were refined against the maps in Phenix-Refine[51] with reference model restraints to the spoked barrel PilQ structures. While side-chains were used to ensure the models made biological sense during model building, they were ultimately removed as the map quality did not justify them being modeled.

Acknowledgements

This work was supported by a grant from the Canadian Institutes for Health Research (CIHR) MOP 93585 to L.L.B. and P.L.H. M.M. was supported by a CIHR Doctoral Studentship and Ontario

Graduate Scholarship during these studies. P.L.H. and J.L.R. are recipients of Canada Research Chairs. The graphics programs used in this study were accessed using SBGrid.

REFERENCES

1. McCallum, M., Burrows, L.L. & Howell, P.L. The Dynamic Structures of the Type IV Pilus. *Microbiol Spectrum* **7**(2019).
2. Craig, L., Forest, K.T. & Maier, B. Type IV pili: dynamics, biophysics and functional consequences. *Nat Rev Microbiol* **17**, 429-440 (2019).
3. Chang, C.Y. Surface Sensing for Biofilm Formation in Pseudomonas aeruginosa. *Front Microbiol* **8**, 2671 (2017).
4. Valentini, M. & Filloux, A. Biofilms and Cyclic di-GMP (c-di-GMP) Signaling: Lessons from Pseudomonas aeruginosa and Other Bacteria. *J Biol Chem* **291**, 12547-55 (2016).
5. Mah, T.F. & O'Toole, G.A. Mechanisms of biofilm resistance to antimicrobial agents. *Trends Microbiol* **9**, 34-9 (2001).
6. McCallum, M., Tammam, S., Khan, A., Burrows, L.L. & Howell, P.L. The molecular mechanism of the type IVa pilus motors. *Nat Commun* **8**, 15091 (2017).
7. McCallum, M. et al. Multiple conformations facilitate PilT function in the type IV pilus. *Nat Commun* **10**, 5198 (2019).
8. Marko, V.A., Kilmury, S.L.N., MacNeil, L.T. & Burrows, L.L. Pseudomonas aeruginosa type IV minor pilins and PilY1 regulate virulence by modulating FimS-AlgR activity. *PLoS Pathog* **14**, e1007074 (2018).
9. Nguyen, Y. et al. Pseudomonas aeruginosa minor pilins prime type IVa pilus assembly and promote surface display of the PilY1 adhesin. *J Biol Chem* **290**, 601-11 (2015).
10. McCallum, M. et al. PilN Binding Modulates the Structure and Binding Partners of the Pseudomonas aeruginosa Type IVa Pilus Protein PilM. *J Biol Chem* **291**, 11003-15 (2016).
11. Tammam, S. et al. PilMNOPQ from the Pseudomonas aeruginosa type IV pilus system form a transenvelope protein interaction network that interacts with PilA. *J Bacteriol* **195**, 2126-35 (2013).
12. Luo, Y. et al. A hierarchical cascade of second messengers regulates Pseudomonas aeruginosa surface behaviors. *mBio* **6**(2015).
13. Persat, A., Inclan, Y.F., Engel, J.N., Stone, H.A. & Gitai, Z. Type IV pili mechanochemically regulate virulence factors in Pseudomonas aeruginosa. *Proc Natl Acad Sci U S A* **112**, 7563-8 (2015).
14. Filloux, A. & Voulhoux, R. Multiple Structures Disclose the Secretins' Secrets. *J Bacteriol* **200**(2018).
15. Worrall, L.J. et al. Near-atomic-resolution cryo-EM analysis of the Salmonella T3S injectisome basal body. *Nature* **540**, 597-601 (2016).
16. Siewering, K. et al. Peptidoglycan-binding protein TsaP functions in surface assembly of type IV pili. *Proc Natl Acad Sci U S A* **111**, E953-61 (2014).
17. Collins, R.F. et al. Structure of the Neisseria meningitidis outer membrane PilQ secretin complex at 12 A resolution. *J Biol Chem* **279**, 39750-6 (2004).

465 18. Koo, J., Lamers, R.P., Rubinstein, J.L., Burrows, L.L. & Howell, P.L. Structure of the
466 Pseudomonas aeruginosa Type IVa Pilus Secretin at 7.4 A. *Structure* **24**, 1778-1787
467 (2016).
468 19. Chang, Y.W. et al. Architecture of the type IVa pilus machine. *Science* **351**, aad2001
469 (2016).
470 20. Weaver, S.J., Sazinsky, M.H., Dalia, T.N., Dalia, A.B. & Jensen, G.J. CryoEM structure
471 of the Vibrio cholerae Type IV competence pilus secretin PilQ. *bioRxiv* (2020).
472 21. D'Imprima, E. et al. Cryo-EM structure of the bifunctional secretin complex of Thermus
473 thermophilus. *Elife* **6**, e30483 (2017).
474 22. Yin, M., Yan, Z. & Li, X. Structural insight into the assembly of the type II secretion
475 system pilotin-secretin complex from enterotoxigenic Escherichia coli. *Nat Microbiol* **3**,
476 581-587 (2018).
477 23. Chernyatina, A.A. & Low, H.H. Core architecture of a bacterial type II secretion system.
478 *Nat Commun* **10**, 5437 (2019).
479 24. Punjani, A., Rubinstein, J.L., Fleet, D.J. & Brubaker, M.A. cryoSPARC: algorithms for
480 rapid unsupervised cryo-EM structure determination. *Nat Methods* **14**, 290-296 (2017).
481 25. Yan, Z., Yin, M., Xu, D., Zhu, Y. & Li, X. Structural insights into the secretin
482 translocation channel in the type II secretion system. *Nat Struct Mol Biol* **24**, 177-183
483 (2017).
484 26. Marks, D.S. et al. Protein 3D structure computed from evolutionary sequence variation.
485 *PLoS One* **6**, e28766 (2011).
486 27. de Juan, D., Pazos, F. & Valencia, A. Emerging methods in protein co-evolution. *Nat Rev*
487 *Genet* **14**, 249-61 (2013).
488 28. Hu, J. et al. Cryo-EM analysis of the T3S injectisome reveals the structure of the needle
489 and open secretin. *Nat Commun* **9**, 3840 (2018).
490 29. Nudleman, E., Wall, D. & Kaiser, D. Polar assembly of the type IV pilus secretin in
491 Myxococcus xanthus. *Mol Microbiol* **60**, 16-29 (2006).
492 30. Wilderman, P.J. et al. Characterization of an endoprotease (PrpL) encoded by a PvdS-
493 regulated gene in Pseudomonas aeruginosa. *Infect Immun* **69**, 5385-94 (2001).
494 31. Michel, G.P., Durand, E. & Filloux, A. XphA/XqhA, a novel GspCD subunit for type II
495 secretion in Pseudomonas aeruginosa. *J Bacteriol* **189**, 3776-83 (2007).
496 32. Terashima, H. et al. Insight into the assembly mechanism in the supramolecular rings of
497 the sodium-driven Vibrio flagellar motor from the structure of FlgT. *Proc Natl Acad Sci*
498 *U S A* **110**, 6133-8 (2013).
499 33. Kelley, L.A., Mezulis, S., Yates, C.M., Wass, M.N. & Sternberg, M.J. The Phyre2 web
500 portal for protein modeling, prediction and analysis. *Nat Protoc* **10**, 845-58 (2015).
501 34. Yang, J. et al. The I-TASSER Suite: protein structure and function prediction. *Nat*
502 *Methods* **12**, 7-8 (2015).
503 35. Jones, C.J. & Wozniak, D.J. Congo Red Stain Identifies Matrix Overproduction and Is an
504 Indirect Measurement for c-di-GMP in Many Species of Bacteria. *Methods Mol Biol*
505 **1657**, 147-156 (2017).
506 36. Vasseur, P., Vallet-Gely, I., Soscia, C., Genin, S. & Filloux, A. The pel genes of the
507 Pseudomonas aeruginosa PAK strain are involved at early and late stages of biofilm
508 formation. *Microbiology* **151**, 985-997 (2005).
509 37. Sokol, P.A., Ohman, D.E. & Iglewski, B.H. A more sensitive plate assay for detection of
510 protease production by Pseudomanas aeruginosa. *J Clin Microbiol* **9**, 538-40 (1979).

38. Ravichandran, A., Ramachandran, M., Suriyanarayanan, T., Wong, C.C. & Swarup, S. Global Regulator MorA Affects Virulence-Associated Protease Secretion in Pseudomonas aeruginosa PAO1. *PLoS One* **10**, e0123805 (2015).
39. Lopez-Baena, F.J., Vinardell, J.M. & Medina, C. Regulation of Protein Secretion Systems Mediated by Cyclic Diguanylate in Plant-Interacting Bacteria. *Front Microbiol* **10**, 1289 (2019).
40. Jain, R., Behrens, A.J., Kaever, V. & Kazmierczak, B.I. Type IV pilus assembly in Pseudomonas aeruginosa over a broad range of cyclic di-GMP concentrations. *J Bacteriol* **194**, 4285-94 (2012).
41. Berry, J.L. et al. Structure and assembly of a trans-periplasmic channel for type IV pili in Neisseria meningitidis. *PLoS Pathog* **8**, e1002923 (2012).
42. de Lorenzo, V. & Timmis, K.N. Analysis and construction of stable phenotypes in gram-negative bacteria with Tn5- and Tn10-derived minitransposons. *Methods Enzymol* **235**, 386-405 (1994).
43. Ha, D.G., Kuchma, S.L. & O'Toole, G.A. Plate-based assay for swarming motility in Pseudomonas aeruginosa. *Methods Mol Biol* **1149**, 67-72 (2014).
44. Turnbull, L. & Whitchurch, C.B. Motility assay: twitching motility. *Methods Mol Biol* **1149**, 73-86 (2014).
45. Schneider, C.A., Rasband, W.S. & Eliceiri, K.W. NIH Image to ImageJ: 25 years of image analysis. *Nat Methods* **9**, 671-5 (2012).
46. Vehlow, C. et al. CMView: interactive contact map visualization and analysis. *Bioinformatics* **27**, 1573-4 (2011).
47. Rubinstein, J.L. & Brubaker, M.A. Alignment of cryo-EM movies of individual particles by optimization of image translations. *J Struct Biol* **192**, 188-95 (2015).
48. Rohou, A. & Grigorieff, N. CTFFIND4: Fast and accurate defocus estimation from electron micrographs. *J Struct Biol* **192**, 216-21 (2015).
49. Punjani, A., Zhang, H., Fleet D. J. Non-uniform refinement: Adaptive regularization improves single particle cryo-EM reconstruction. *bioRxiv* (2019).
50. Casanal, A., Lohkamp, B. & Emsley, P. Current Developments in Coot for Macromolecular Model Building of Electron Cryo-microscopy and Crystallographic Data. *Protein Sci* (2019).
51. Afonine, P.V. et al. Real-space refinement in PHENIX for cryo-EM and crystallography. *Acta Crystallogr D Struct Biol* **74**, 531-544 (2018).

Figure Legends

Figure 1. Electron cryomicroscopy of PilQ from *P. aeruginosa* reveals multiple conformers. **A-C,** Map (upper left) and model (upper right) of $PilQ^{Pa}$ (coloured) with additional spoke and plug density (black). Top (top), side (middle), and cross section (bottom) views are shown. **A,** Map and model of spoked tetradecameric $PilQ^{Pa}$ (purple). **B,** Map and model of tetradecameric $PilQ^{Pa}$ without spokes (teal). **C,** Map and model of pentadecameric $PilQ^{Pa}$ (orange). **D,** Evolutionarily coupled residues in PilQ (gray) are compared with the structure of $PilQ^{Pa}$. Residue

553 pairs that are within 8 Å of each other in the tertiary structure of $PilQ^{Pa}$ are shown (black).
554 Residue pairs that are within 8 Å of each other between $PilQ^{Pa}$ protomers are also shown (gold).
555 Specific evolutionarily coupled residues that are not supported by the $PilQ^{Pa}$ structure are noted
556 with coloured arrows: G554-P635 (yellow), E663-A624 (red), T538-E652 (green), L545-T653
557 (magenta), and L546-V457 (blue). **E**, Location of the G554-P635 and E663-A624 residue pairs,
558 as well as hinge residue G577 (asterisk), on a cross section of $PilQ^{Pa}$ (left) and a model for
559 secretin gate opening consistent with these co-evolved residues. **F**, Location of the T538-E652,
560 L545-T653, and L546-V457 residue pairs on $PilQ^{Pa}$ (left) and a model for secretin barrel folding
561 consistent with these co-evolved residues. **G,** Surface representation of conserved residues (top)
562 and electrostatic potential (bottom) in $PilQ^{Pa}$. **H,** Structure alignment of monomers from the
563 spoked tetradecameric $PilQ^{Pa}$ (purple), tetradecameric $PilQ^{Pa}$ with no spokes (teal), and
564 pentadecameric $PilQ^{Pa}$ (orange) models. Grey square with black PilQ cartoon has a dotted red
565 box highlighting area of PilQ shown. Structural differences are highlighted (arrows) and the pivot
566 point for these differences is noted (black circle). **I,** Cartoon model summarizing the differences
567 between the three $PilQ^{Pa}$ structures determined. Pentadecameric $PilQ^{Pa}$ (orange) is wider and has
568 more horizontal secretin gates compared to the other structures. Tetradecameric $PilQ^{Pa}$ (teal) has
569 invaginated secretin gates and partial plug density (black triangle). Spoked tetradecameric $PilQ^{Pa}$
570 (purple) has further invaginated secretin gates, plug density (black triangle), and spokes (black
571 circles).
572
573 **Figure 2. TsaP can be modeled in the PilQ spoke density as a heptameric ring. A,** TsaP
574 domain model predictions: the I-Tasser prediction of the CI domain (residues 126-211)[34] and the
575 Phyre[2] prediction of the CII domain (residues 235-324)[33]. **B,** Evolutionarily coupled residues in
576 TsaP (gray) are compared with the structure of the C-terminal 224 residues of TsaP. Residue
577 pairs that are within 8 Å of each other are shown from the CI domain (yellow), the CII domain
578 (wheat-yellow), and the linkers preceding and following the CI domain (brown). Intramolecular
579 and intermolecular contacts in the TsaP structure between the CI and CII domains are also shown
580 (blue and red, respectively). **C-D,** Map (top), model (middle), and cartoon (bottom) summarizing
581 the structure of TsaP. Zoomed-in (**C**) and zoomed-out (**D**) views are shown. TsaP is coloured as
582 in **B**; PilQ is shown in grey (**C**) or purple (**D**).
583

584 **Figure 3. TsaP over-expression induces cyclic di-GMP up-regulation.** Wild-type *P. aeruginosa*
585 (left), the *tsaP* mutant (center left), *P. aeruginosa* expressing TsaP (center right), and the *tsaP*
586 mutant expressing TsaP (right). **A,** Twitching motility was assayed by crystal violet staining and
587 the areas traversed by the bacteria were measured (violin plot with individual measurements shown
588 as empty circles; n = 7 for Wild-type with and without vector, n = 6 for the *tsaP* mutant with and
589 without vector; data are representative of three independent trials). Mean twitching areas were
590 compared to wild type plus the control vector at the corresponding arabinose concentration with
591 the two-way ANOVA test; p-values are reported. **B**, Representative crystal violet stained twitching
592 motility zones (top), Congo-red agar colonies (middle), and skim milk agar colonies (bottom) are
593 shown for 0 % arabinose induction (-) or 0.1% arabinose induction (++). **C**, Luminescence over
594 time relative to uninduced control without arabinose (top), with luciferase expression under the
595 control of the cyclic di-GMP inducible *cdrA* promotor. Mean luminescence (n=3, representative of
596 three independent trials) relative to a matched uninduced control is shown for 0.1% arabinose
597 induction (orange, ++) or 0.01% arabinose induction (beige, +) as a filled in line with the standard
598 error of the mean (dotted lines). Growth measured by absorbance at 600nm over time of liquid
599 cultures (bottom). Mean growth (n=3, representative of three independent trials) is shown for 0 %
600 arabinose induction (gray, -), 0.01% arabinose induction (beige, +), or 0.1 % arabinose induction
601 (orange, ++) with the standard error of the mean shown (dotted lines). **D**, Congo red dye uptake
602 assay of PAO1 (wild-type), PAO1::*pilN*, PAO1::*pilO*, PAO1::*pilP*, PAO1::*pilQ*, PAO1::*pilA*,
603 PAO1::*pilF* and PAO1::*pilY1* with (++) and without (-) TsaP overexpression.
604
605
606

607 Figure 1

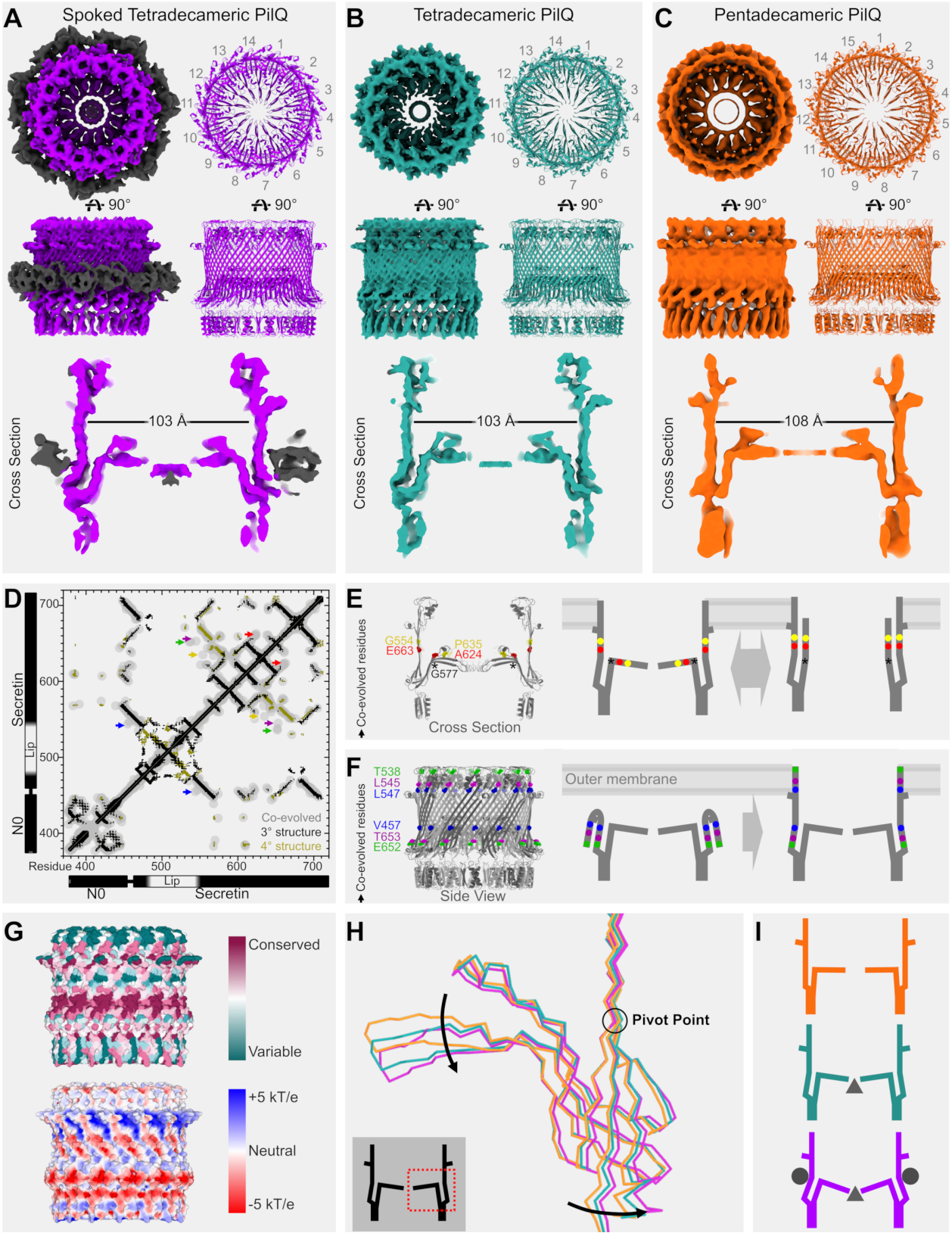

608

609 Figure 2

610

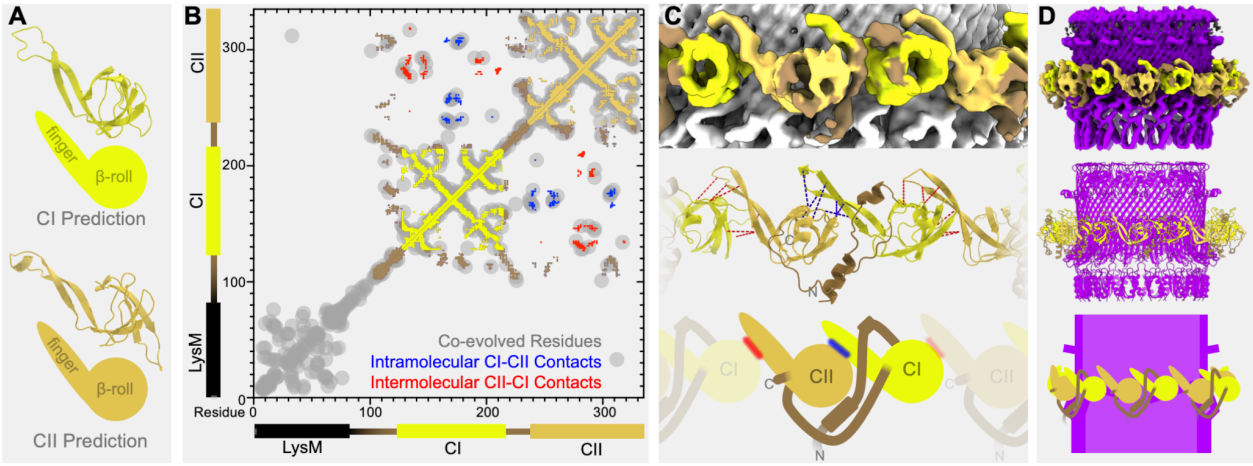

611

612 Figure 3

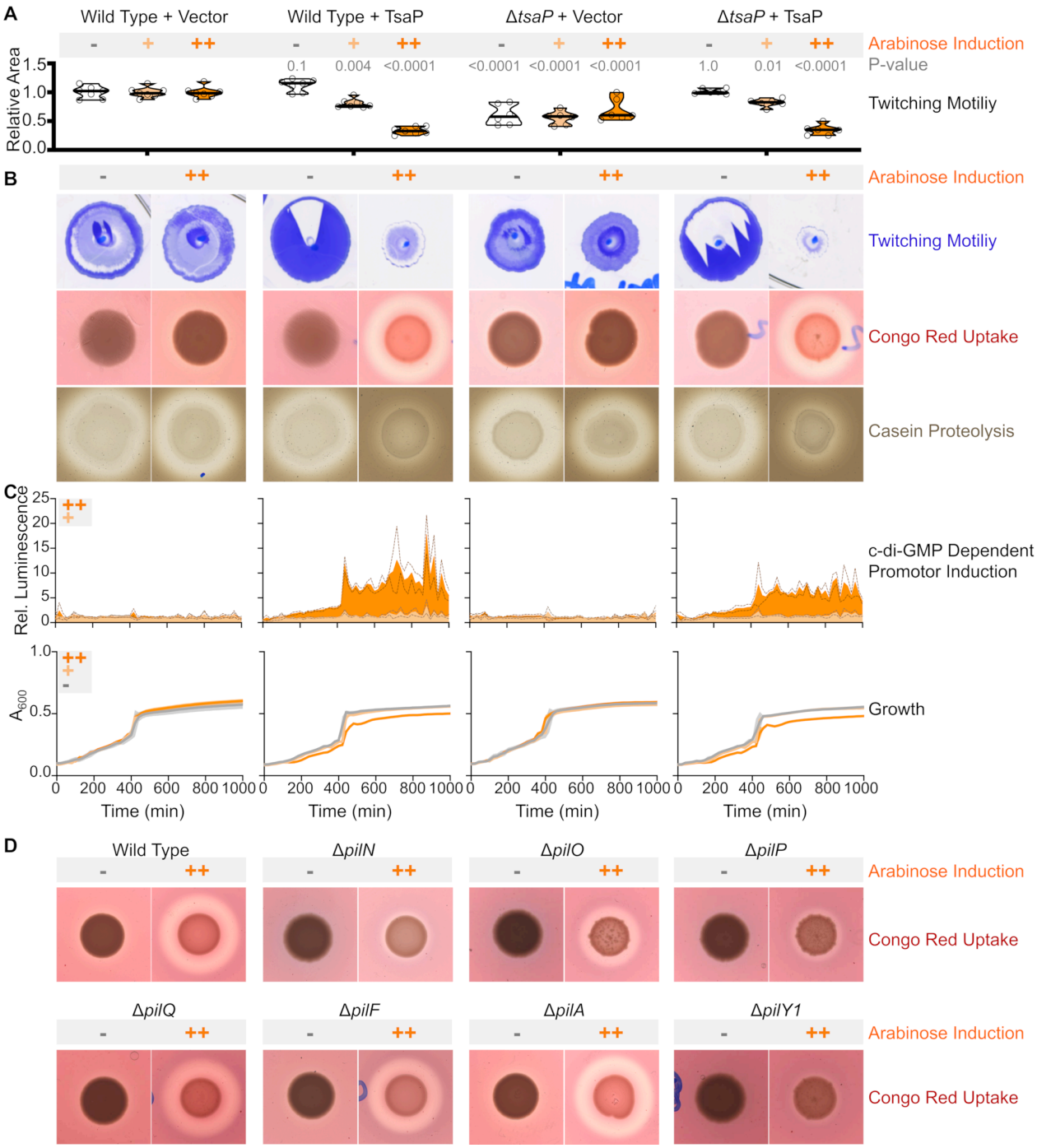

613